Cold-Atom Buoy: A Differential Magnetic Sensing Technique in Cold Quadrupole Traps

Árpád Kurkó¹, Dávid Nagy¹, Alexandra Simon¹, Thomas W. Clark¹, András Dombi¹, Dániel Varga¹, Francis B. Williams¹, József Fortágh², Peter Domokos¹ András Vukics^{1*}

¹HUN-REN Wigner Research Centre for Physics, Konkoly-Thege M. út 29-33, Budapest, 1121, Hungary.

²Center for Quantum Science, Physikalisches Institut, Eberhard Karls Universität Tübingen, Auf der Morgenstelle 14, Tübingen, 72076, Germany.

*Corresponding author(s). E-mail(s): vukics.andras@wigner.hun-ren.hu;

Abstract

We present a technique for vectorial magnetic sensing using a cold-atom cloud trapped in a magnetic quadrupole. The center of the trapped cloud is determined by absorption imaging and compared for opposite polarities of the quadrupole. In the presence of an external magnetic field, the displacement of the cloud depends on both the field's direction and magnitude. By analyzing this shift under polarity reversal, we infer the two transverse components of a homogeneous external magnetic field relative to the imaging axis, without requiring spectroscopic interrogation. Assuming micron-scale position sensitivity and typical magnetic field gradients, the method enables resolution at the milli-Gauss level. It is compatible with standard cold-atom setups and offers a practical tool for field compensation in magnetically sensitive experimental stages. As such, it establishes a bridge between traditional macroscopic magnetic field probes and atomic-physics-based precision sensors.

Keywords: cold atoms, quantum sensing, magnetic trapping, magnetic sensing, differential metrology

1 Introduction

Magnetic trapping is a foundational technique in cold-atom physics, enabling conservative, long-duration confinement of neutral atoms in magnetically sensitive internal states [1]. Following the advent of magneto-optical traps (MOTs) [2], the development of purely magnetic traps allowed atomic ensembles to be held and manipulated without continuous optical scattering. This led to the first observations of Bose–Einstein condensation [3, 4] and has since underpinned advances in quantum simulation, interferometry, and hybrid quantum systems [5–7]. The canonical magnetic trap geometries – such as the quadrupole and the Ioffe–Pritchard configuration – are typically realized using either macroscopic coils mounted near or inside the vacuum chamber, or micrometer-scale current paths on atom chips [8–10]. These setups exploit the spatial dependence of the magnetic field near the trap center to create a potential minimum for low-field-seeking Zeeman states. A central advantage of such magnetic traps is that they are easy to configure (e.g. displace) via the feed current of the electromagnets [11–14].

Atomic systems account for some of the most sensitive [15–17] and accurate [18] means of magnetic field measurement, having become competitive with superconducting quantum interference devices [19]. These sensors rely on the internal degrees of freedom of atoms – typically hyperfine Zeeman sublevels – and detect magnetic fields through their influence on atomic spin precession via the optical response [20]. A wide variety of architectures exist, from thermal atomic beams in early precision experiments [21], to spin-exchange relaxation-free magnetometers based on alkali vapors [22–26]. More recently, to laser-cooled atomic ensembles in vacuo [27, 28], all-optical multi-axis measurement [29]; and all-optical, multi-dimensional magnetic measurement using spatially shaped beams [30].

In this work, we introduce a technique for magnetic field sensing based on the spatial displacement of a cold-atom cloud held in a magnetic quadrupole trap and manipulated exclusively with changes in current. By alternating the polarity of the quadrupole field between consecutive experimental shots, we generate a symmetric displacement response of the trap center in the presence of an external homogeneous magnetic field. This effect is measured using absorption imaging and two-dimensional Gaussian fitting of the atom cloud's optical depth profile.

The method is remarkably simple: it relies solely on spatial degrees of freedom and requires no spectroscopic interrogation, microwave fields, or internal-state coherence – making it broadly applicable in settings where magnetic field control is critical but conventional magnetometry is impractical, as for magnetic compensation in coldatom preparation stages. We show that this approach enables vectorial detection of stray magnetic fields transverse to the imaging axis with milli-Gauss-level sensitivity, using standard cold-atom infrastructure. Relying on just a single imaging beam, the method can facilitate portable [31, 32] and miniature [33–35] devices in cold-atom-based quantum technologies.

The strategy of reversing a controlled experimental parameter to reveal or isolate physical effects is a cornerstone of precision metrology. It appears across a wide range of domains: in spin-echo and Ramsey spectroscopy sequences that cancel quasi-static dephasing [36, 37]; in electric dipole moment searches where field polarity is flipped

to isolate parity-violating signatures [38]; and in Pound-Drever-Hall spectroscopy [39] where opposite-sign phase shifts of sidebands cancel in the midpoint of a spectral feature. These differential schemes amplify antisymmetric responses while canceling common-mode drifts and offsets, enabling high-precision measurements in the presence of substantial technical noise. The cold-atom buoy technique follows this paradigm by alternating the sign of the quadrupole gradient between consecutive experimental shots to reverse the geometric response of the trap to external homogeneous magnetic fields. The resulting displacement difference forms a direct observable that scales linearly with the external field.

2 Concept

2.1 Scheme

The potential in a magnetic trap acting on an atom in a magnetic sublevel m_F reads:

$$U(\mathbf{r}) = \mu_{\rm B} q_F m_F |\mathbf{B}(\mathbf{r})|,\tag{1}$$

where $\mu_{\rm B}$ is the Bohr magneton, and g_F is the hyperfine Landé g-factor. The potential being proportional to the modulus of the magnetic field shows that the trapping is independent of the polarity of the quadrupole, in sharp contrast to the MOT stage, where the quadrupole polarity has to match the polarization of the inbound MOT beams.

The response to a homogeneous field, on the other hand, does depend on the quadrupole polarity, and is opposite for opposite quadrupole polarities, forming the basis of the buoy effect. This can be seen by writing the quadrupole field in the following form:

$$\mathbf{B}_{\mathbf{Q}}(\mathbf{r}) = Q(\mathbf{x} + \mathbf{y} - 2\mathbf{z}), \quad Q \equiv \hat{\mathbf{x}} \cdot \partial_x \mathbf{B}(\mathbf{r})|_{\mathbf{r} - \epsilon \hat{\mathbf{x}}}$$
 (2)

where Q is the strength of the quadrupole, considered a signed scalar quantity, that can be expressed via the gradient of the field in one of the Cartesian directions at an infinitesimal distance ϵ from the center. This is a good approximation of the magnetic field of a coil pair with opposite driving currents in the vicinity of the geometrical midpoint between the coils, cf. section 3.4.

While this form of the field leads to a potential with its minimum at $\mathbf{r} = 0$, where $\mathbf{B}_{\mathrm{Q}} = 0$, the superposition of a homogeneous external field $\mathbf{B}_{\mathrm{ext}}$ displaces this zero-field point to

$$\mathbf{r}_0 = \frac{\left[\hat{\mathbf{z}} \circ \hat{\mathbf{z}} - 2(\hat{\mathbf{x}} \circ \hat{\mathbf{x}} + \hat{\mathbf{y}} \circ \hat{\mathbf{y}})\right] \mathbf{B}_{\text{ext}}}{2Q},$$
(3)

changing sign with Q. The sign of Q corresponds to the quadrupole polarity: positive when the axial field gradient points inward along +z, and negative otherwise. Assuming perfectly balanced driving of the two coils making up the quadrupole, Q is proportional to the driving current, so its sign can be flipped simply by flipping the direction of the drive current.

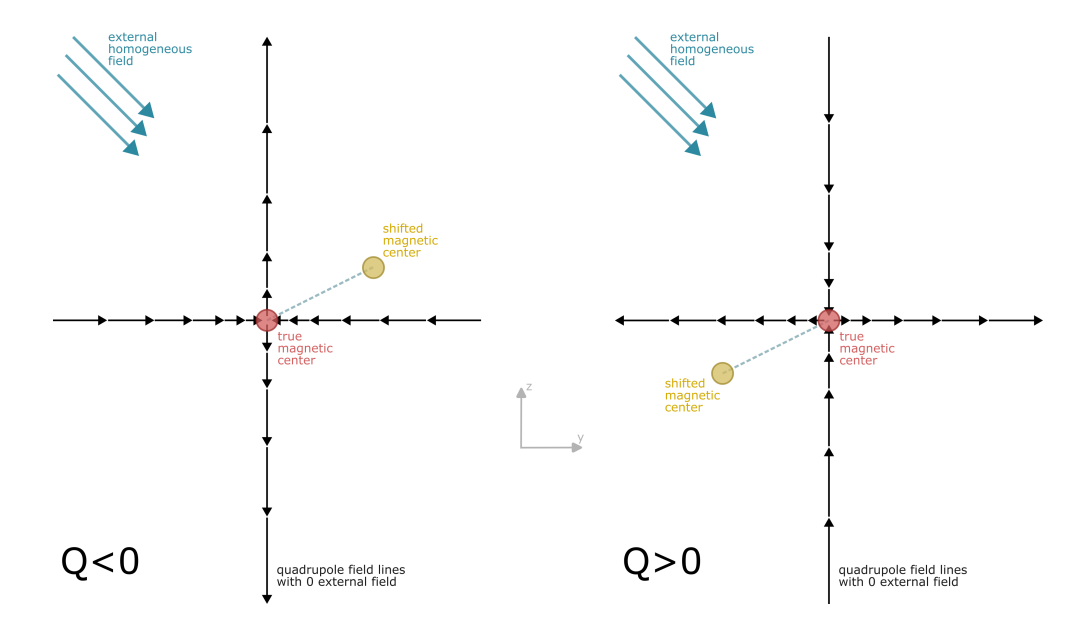


Fig. 1 Schematic of the cold-atom buoy concept. In the quadrupole configuration, the magnetic field grows linearly in the three Cartesian directions with the distance from the center (with opposite sign and doubled gradient in the vertical direction). This makes that an external homogeneous field shifts the center of the quadrupole (the $\mathbf{B}=0$ point – denoted with orange) with the same distance, but opposite directions from the true geometrical center (denoted with red) under a switch of quadrupole polarity. For the definition of Q, cf. eq. (2). The buoy analogy is based on the identification of the shifting cold-atom cloud with the buoy floating on the surface of the water (the plane transverse to the imaging axis), and the true (zero-external-field) magnetic center with the anchor point of the buoy. The external field is the current that displaces the buoy.

Equation (3) condenses the cold-atom buoy effect, cf. fig. 1: \mathbf{r}_0 flips sign by Q flipping sign, and depends linearly and directionally on $\mathbf{B}_{\mathrm{ext}}$. The magnetic zero being the minimum of the potential is designated by the point of maximum density of the trapped atomic cloud, that can be determined by absorption imaging.

Importantly, the cold-atom buoy is a purely geometric effect that relies on the linear directional dependence of the field (2) in a quadrupole trap, in contrast to a magneto-optical trap, where the interplay between magnetism and light forces sets a much more complex scenario.

2.2 Demonstration

The following experiments are performed in a rubidium-87 cold-atom system, described in section 3.1. To experimentally characterize the buoy effect, the external homogeneous field in all three spatial directions is varied systematically. For this, we vary the currents in three coil pairs operated in the dipole configuration leading to closely homogeneous fields close to the geometrical center of the pairs that coincides with the center of the magnetic quadrupole. The external homogeneous field can

$$\mathbf{B}_{\text{ext}} = \mathbf{B}_{\text{strav}} + \mathbf{B}_{\text{bias}}(I_x, I_y, I_z), \tag{4}$$

where $\mathbf{B}_{\text{stray}}$ encompasses fields not controlled by us, stemming from the Earth and nearby devices.

The shifted quadrupole center is determined by absorption imaging [40, 41] of the magnetically trapped cloud, for details cf. section 3.2. For every setting of the currents (I_x, I_y, I_z) , we record absorption images for both positive and negative quadrupole polarities, and observe the corresponding cloud displacement. The midpoint between the two positions then serves as an estimate of the true magnetic center, i.e., the location of the trap minimum in the absence of external fields.

In its pure form, the buoy effect enables sensing in the two directions transverse to the imaging axis which here is denoted by x. Moreover, according to eq. (3), the displacement in each Cartesian direction is solely determined by the corresponding component of the external field; e.g., displacement along x reflects only $B_{\text{ext},x}$, and so forth. Therefore, given a single imaging axis x, we gain information about the y and z components by varying the currents corresponding to those two directions.

Figure 2 presents data obtained across a broad range of applied compensation currents (I_y, I_z) . Here, we performed 50 experimental shots per (I_y, I_z) pair and quadrupole polarity. The figure shows the absorption imaging field of view. Each small triangle represents the center-of-mass position of the magnetically trapped cloud in a single shot, extracted via a 2D Gaussian fit to the optical density (OD) map, cf. section 3.2. The color indicates the particular (I_y, I_z) setting, while the triangle orientation (upward or downward) denotes the quadrupole polarity. Large triangles show the shot-averaged positions for each condition. The results clearly exhibit the buoy effect:

- 1. For each (I_y, I_z) setting, the cloud positions corresponding to the two quadrupole polarities are averaged separately (large triangles). The midpoint of the segment connecting these two averages (opposite triangle orientations) yields the true magnetic trap center that is, the position of zero total external field. This inferred center is marked by a large rhombus, and it remains nearly invariant across different compensation current settings, as expected. The tight clustering of rhombuses confirms that the differential technique isolates the true magnetic center, independent of the externally applied fields.
- 2. Varying I_y causes horizontal displacement, while varying I_z results in vertical displacement, confirming the expected directional response, although some residual displacement is observed in the orthogonal direction.

This latter imperfection can be attributed to two main sources:

Non-axial imaging alignment: The imaging axis does not perfectly coincide with the laboratory x-axis. As a result, purely horizontal displacements of the cloud project with a small component onto the vertical image coordinate, and vice versa, which contributes to slight apparent cross-coupling in the displayed displacements.

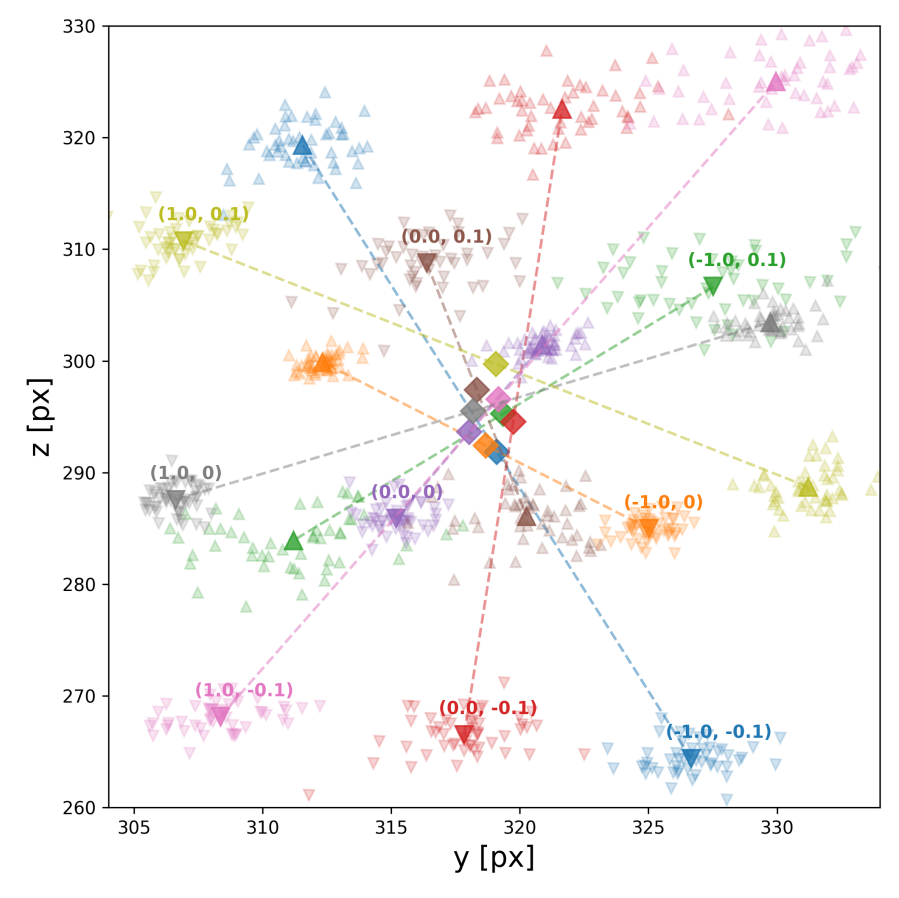


Fig. 2 Demonstration of the buoy effect. Positions of the magnetically trapped cloud for various settings of the applied bias currents (I_y,I_z) , displayed in color code on the (y,z) image plane in the field of view of absorption imaging, measured in CCD pixels. For each (I_y,I_z) pair and each quadrupole polarity, 50 absorption images were recorded. Small triangular markers indicate the center-of-mass position of the cloud extracted from a two-dimensional Gaussian fit of each individual absorption image. Upward- and downward-pointing triangles denote shots with opposite quadrupole polarities. The identically colored label (I_y,I_z) at each cloud cluster indicates the applied current pair in ampere for that dataset. For each (I_y,I_z) pair, the cluster centers corresponding to the two quadrupole polarities – denoted by identical, but larger triangles – are connected by a dashed line segment. The midpoint of this segment (shown as a large rhombus of the same color) is the inferred field-compensated magnetic trap center. The difference between the scale of the currents I_y vs. I_z stems from the different geometry of the corresponding coil pairs, cf. section 3.1.

Inhomogeneities of the stray field: Residual magnetic fields near the quadrupole center are not perfectly homogeneous and cannot be fully compensated by bias coils. The effect of inhomogeneities is analyzed in section 3.3.

Figure 3 presents results across a finer range of I_y and I_z values centered around the compensation currents that can be inferred from fig. 2. Here, 100 experimental

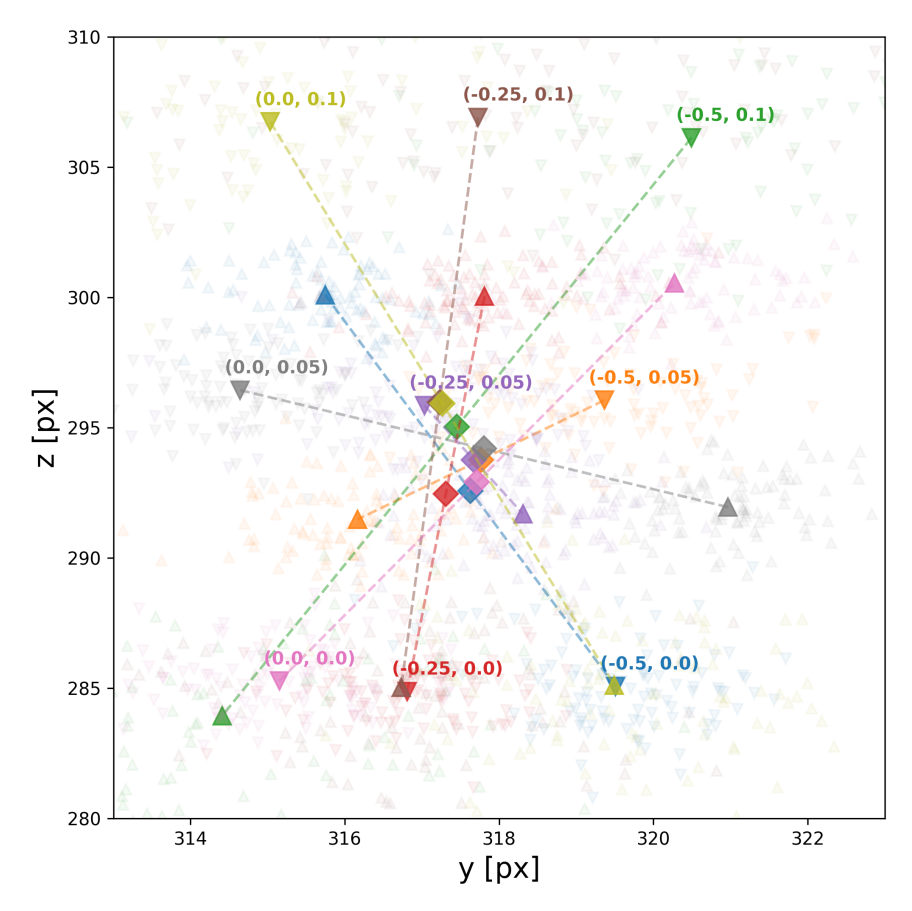


Fig. 3 Zoomed-in displacement data around the compensation point. Same measurement as in fig. 2, but recorded over a finer grid of I_y and I_z values centered around the compensation currents inferred from that figure. Here, 100 shots were taken for each current pair and quadrupole polarity. This finer sampling allows for a more precise localization of the true magnetic center corresponding to $\mathbf{B}_{\text{ext}} = 0$, and provides further validation of the buoy effect at higher resolution.

shots were taken for each condition and polarity. This finer sampling enables a more precise identification of the true magnetic center corresponding to $\mathbf{B}_{\mathrm{ext}} = 0$.

Next, exploiting the directional and linear response of the cloud displacement to the total external field $\mathbf{B}_{\mathrm{ext}}$, as given by (3), and the linear dependence of the controlled bias field $\mathbf{B}_{\mathrm{bias}}$ on the applied coil currents, we infer the compensation currents that zero the net external field in each direction via linear regression. That is, according to the Biot–Savart law, we can write

$$\mathbf{B}_{\text{bias}} = \hat{\mathbf{x}} \, \alpha_x I_x + \hat{\mathbf{y}} \, \alpha_y I_y + \hat{\mathbf{z}} \, \alpha_z I_z, \tag{5}$$

where the coefficients α_i characterize the effective field contributions of the corresponding coil pair at the MOT center. Compensation means finding the currents

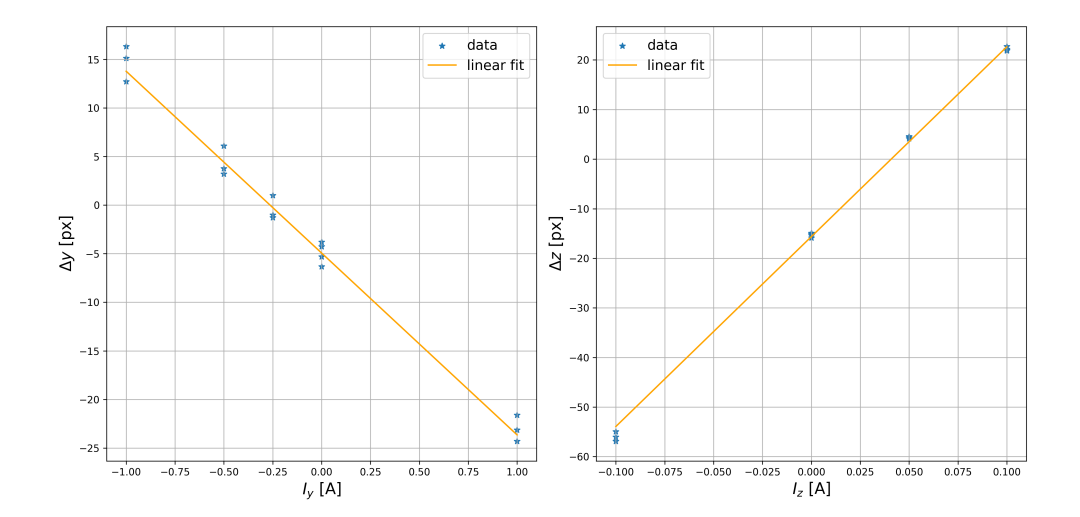


Fig. 4 Finding the correct compensation Displacement of the cluster centers under polarity reversal as a function of the applied currents I_y and I_z , extracted from the large triangle positions in figs. 2 and 3. The correct compensation current I_y (I_z) is the zero-crossing – the $\Delta y=0$ ($\Delta z=0$) point – of the fitted linear function plotted as an orange line in each panel.

where

$$\mathbf{B}_{\text{bias}}(I_x^{@}, I_y^{@}, I_z^{@}) = -\mathbf{B}_{\text{stray}} \quad \text{i.e.} \quad I_x^{@} = -\frac{\hat{\mathbf{x}} \cdot \mathbf{B}_{\text{stray}}}{\alpha_x}, \quad \text{etc.}$$
 (6)

Figure 4 illustrates these considerations. The data is aggregated from both datasets presented in figs. 2 and 3, the displacement of the center under quadrupole polarity reversal for a given compensation setting defined as the difference between the positions of the large triangles of the same color but opposite orientation. A linear model can be fitted, whose zero crossings indicate the correct compensation currents as $I_y^@=-0.27\,\mathrm{A}$ and $I_z^@=0.035\,\mathrm{A}$. The stopping of the buoy, that is, the independence of the trap center on quadrupole polarity in case of $\mathbf{B}_{\mathrm{ext}}=0$ is further demonstrated in fig. 5.

2.3 Precision

To estimate the precision of the cold-atom buoy method, we need to address how precisely the center of a magnetically trapped cold ensemble can be determined, since the method is based on identifying this with the center of the quadrupole itself – which is possibly shifted by external fields. Any uncertainty in position can be directly translated to an uncertainty of magnetic field via the known quadrupole field strength, whose unit is magnetic field per unit length.

The uncertainty of the cloud center has statistical and systematic components. The former can be decreased by increasing the statistical ensemble that we use for averaging, while the second can manifest in different magnitudes on different time scales. The interplay of these errors can be demonstrated with the Allan deviation used in various cold-atom contexts [42–44].

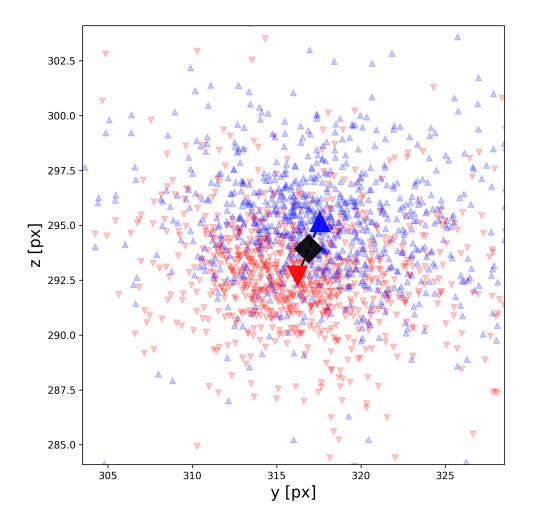


Fig. 5 The stopping of the buoy at the compensation currents determined in fig. 4, $I_y^{@} = -0.27\,\mathrm{A}$ and $I_z^{@} = 0.035\,\mathrm{A}$. The figure shows the absorption imaging field of view with cloud centers stemming from individual experimental shots with alternating quadrupole polarities indicated with small triangles of opposite orientation as in figs. 2 and 3, with the large triangles and the rhombus having the same meaning as in those figures as well. Here, for the sake of visualizing the two largely overlapping ensembles, we used red and blue colors for plotting the opposite polarities.

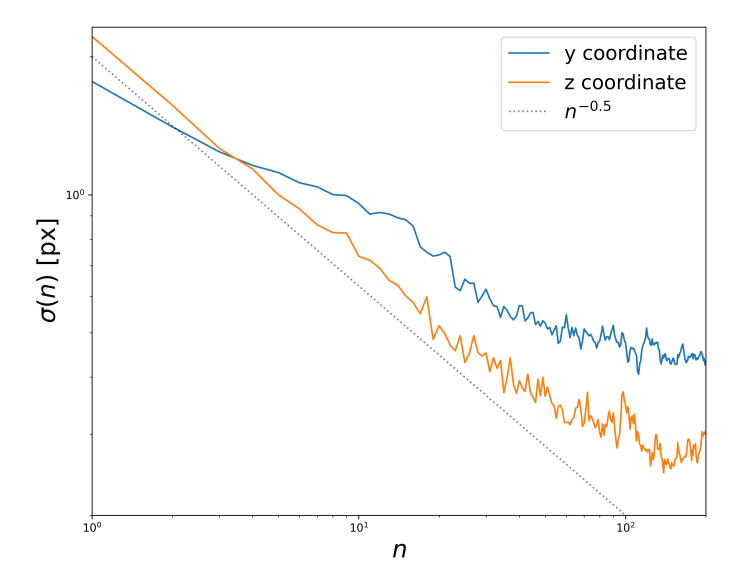


Fig. 6 Non-overlapping Allan deviation. Statistical uncertainty of the determination of the cloud center as a function of ensemble size n, indicating the noise floor in our present system.

An example is shown in fig. 6, where data from a 12-hour-long measurement campaign is compiled. This ensemble of shots is partitioned into non-overlapping ensembles of size n increasing from 1 to 200. The ensemble averages are calculated, and the standard deviation $\sigma(n)$ of these averages across ensembles is taken. In the log-log figure we indicated with dotted line the $n^{-0.5}$ dependence, whose slope corresponds to pure uncorrelated noise. While the uncertainty of the z coordinate follows this initially, that of the y coordinate has smaller initial slope, indicating systematic correlations in the noise, probably stemming from a periodic oscillation in the experimental system whose frequency becomes aliased due to the repetition rate of the experimental cycle.

Eventually both curves flatten into their respective noise floors. Since this is about twice as high in the y direction (0.4 px) than in the z direction, whereas the y gradient of the quadrupole field is half the z gradient, the same uncertainty is obtained for the field. Given the CCD pixel size of 5 µm, the uncertainty of the y coordinate of the center is $\sim 2 \, \mu m$. The quadrupole gradient in these experiments were 2.5 $\frac{G}{mm}$, so the inferred field strength uncertainty reads

$$\Delta B = \frac{\partial B}{\partial y} \Delta y \sim 5 \,\text{mG}. \tag{7}$$

Ideally, all rhombus markers – representing the inferred magnetic centers for different compensation current settings – should coincide, since they correspond to the true quadrupole center in the absence of external fields. Thanks to the differential nature of the buoy method, the statistical uncertainty of these rhombus positions is reduced by a factor of $\sqrt{2}$ assuming uncorrelated noise in the large-triangle averages for opposite quadrupole polarities. Nevertheless, the actual spread of rhombus positions observed in figs. 2 and 3 reflects not only the $\sigma(n)$ uncertainty of the cloud center, but also additional systematics introduced by the variation of the compensation currents. In particular, settings far from optimal compensation degrade the MOT loading and influence the atom number and temperature, thereby altering the cloud dynamics in the magnetic trap and biasing the inferred center position.

2.4 Discussion

The measurements presented here achieving sub-10 mG precision were performed without any specific optimization for metrological performance; they simply relied on our standard cold-atom stage and imaging configuration. We expect that another order of magnitude could be straightforwardly gained by improvements listed below.

First, the effect of gravity should be incorporated into the analysis. Gravity does not alter the position of the minimum of the potential; rather, it renders the potential asymmetric: the gradient in the downward z direction is smaller than in the upward. This results in a skewed cloud, making that the cloud center in terms of optical density does not coincide with the minimum of the potential.

In this work, the cloud center was determined by a full 2-dimensional Gaussian fit, which we preferred owing to its extreme robustness, but which cannot account for skewness and hence the effect of gravity. This usage was based on the assumption that is fundamental to the very buoy effect, cf. eq. (3), namely, that the quadrupole

strength doesn't change on the length scale of the displacement by the external field. The quadrupole strength alone determines the distortion of the shape of the potential by gravity, and hence the skewness and the difference between the cloud center and the magnetic center. I.e., gravity is assumed to amount merely to a constant shift in the downward z direction in figs. 2 and 3.

Second, the statistical analysis can be improved. In this work, we employed a simple arithmetic mean to determine the average center position, i.e., the large triangles in figs. 2, 3 and 5. While straightforward, this approach is sensitive to statistical outliers and may not represent the optimal center estimator under all conditions. To increase robustness against outliers [45], alternative methods such as sigma clipping [46], Chauvenet rejection [47], or the Huber M-estimator [48] could be adopted.

In this connection we note that if the aim is restricted to sensing external fields – specifically, detecting whether any displacement occurs under quadrupole polarity reversal – the analysis can be simplified further. In such cases, unsupervised clustering methods such as k-means [49, 50] can be the choice to efficiently identify polarity-separated clusters. Conversely, if the aim is to find the correct compensation, we may not need large ensembles as in section 2.2. Instead, we can iterate via Bayesian regression [46, 51, 52], feeding information directly into a linear fit similar to fig. 4.

Calibration of the buoy method to real units can be achieved analogously to the error estimation procedure above. As detailed in section 3.4, we have a precise numerical model of the electromagnet configuration that allows for calculating the field in real units at any point within the experimental volume. By combining this with the known pixel size of the CCD we establish a direct correspondence in real units between field gradients and cloud displacements.

Finally, although the buoy method works a priori in the two dimensions transverse to the imaging axis, it is possible to obtain information about the third dimension by introducing a known inhomogeneous field. As shown in section 3.3, inhomogeneities in general couple the spatial dimensions. In our geometry, a single current-carrying wire aligned vertically and situated close to the MOT center could couple the response to the x-component of the external field into the y-z imaging plane. By switching the direction of the current in this wire together with switching the polarity of the quadrupole, we could recover the ideal buoy effect, but with information about the third dimension as well.

3 Methods

3.1 System and protocol

The experimental system is a rubidium-87 cold-atom system sketched in fig. 7. The coils responsible for generating the MOT magnetic fields are mounted inside the vacuum chamber, allowing operation with relatively low currents – up to $5\,\mathrm{A}$ – for which ultra-precise current sources are available. The same in-vacuum MOT coil pair is also used for generating the magnetic quadrupole trap in a subsequent stage. The internal radius of the MOT coils is $32\,\mathrm{mm}$, their width $16\,\mathrm{mm}$, their thickness $10\,\mathrm{mm}$, and they are separated vertically by $34\,\mathrm{mm}$.

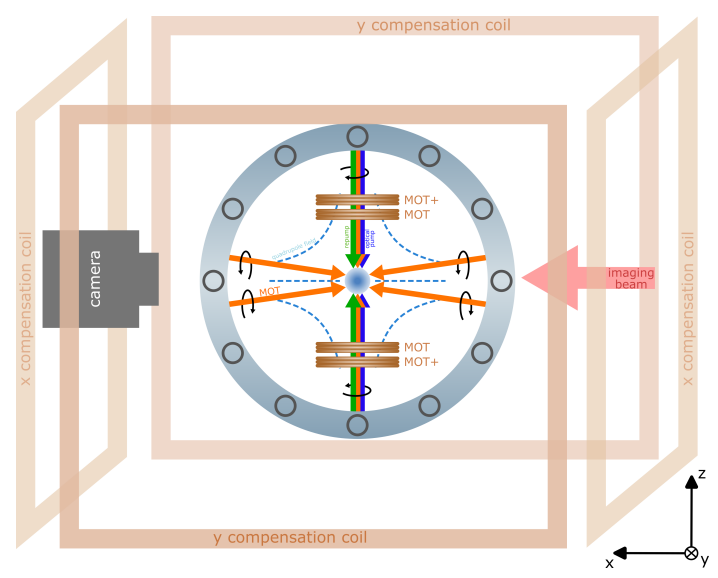


Fig. 7 The experimental setup. The schematic viewport represents the vacuum chamber. The large rectangular loops around the chamber show the configuration of the external compensation coils along the x and y directions. Compensation in the z direction is provided by an additional intravacuo coil pair labeled MOT+.

The experimental protocol proceeds as follows. After a MOT loading stage on the $F=2\leftrightarrow F'=3$ transition of the D_2 line, the magnetic quadrupole field is turned off, and polarization gradient cooling (PGC) is applied in the circ/circ configuration using the same optical beams as for the MOT. We then extinguish the MOT beams, retain only the repumper addressing the F=1 ground state, and apply optical pumping on the $F=2\leftrightarrow F'=2$ transition in the presence of a small homogeneous magnetic field. This field defines the quantization axis and enables population transfer into the low-field-seeking Zeeman sublevel $F=2, m_F=2$.

Subsequently, a strong quadrupole magnetic trap is ramped up gradually – satisfying the adiabaticity condition – to an axial gradient of 5 to 6.6 $\frac{G}{mm}$. After the trap reaches full strength, we wait for 400 ms to allow the atomic cloud to relax; that is, to damp center-of-mass and breathing oscillations before image acquisition.

An important technical detail concerns the rubidium dispenser located approximately 1.5 cm from the MOT center. To minimize perturbations from its stray inhomogeneous magnetic field – arising from the current in its leads – the dispenser is operated in pulsed mode and switched off shortly before the end of the MOT collection stage. This prevents it from interfering with the buoy effect during the sensitive magnetic trapping phase. For full details of the setup and the experimental protocol cf. [53].

The magnetic trap provides an adiabatic potential since the atomic dipole has to follow the direction of the magnetic field at the position of the atom in order to remain in the low-field seeking state. Put otherwise, the parametric evolution (with parameter **r**) of the Hamiltonian of the internal atomic dynamics has to remain adiabatic in order

for the state to remain in $F=2, m_F=2$. The potential (1) can be derived as:

$$U(\mathbf{r}) = -\boldsymbol{\mu} \cdot \mathbf{B}(\mathbf{r}) \approx -\left(-\mu_{\mathrm{B}} g_F m_F \frac{\mathbf{B}(\mathbf{r})}{|\mathbf{B}(\mathbf{r})|}\right) \cdot \mathbf{B}(\mathbf{r}) = \mu_{\mathrm{B}} g_F m_F |\mathbf{B}(\mathbf{r})|, \tag{8}$$

where the second, approximate equality expresses the adiabatic and the linear Zeeman conditions, whereas the sign of μ reflects that of the low-field seeking state.

The three pairs of coils used to generate the compensation field (5) consist of (cf. fig. 7)

- two large pairs dubbed compensation coils and mounted outside the vacuum chamber with their axes along the two horizontal directions (x and y)
- an intra-vacuo pair dubbed MOT+ and mounted just outside of the MOT coil pair with its axis along the z direction. They have the same geometry as the MOT coils, but are separated by 74 mm

In eq. (4), I_x and I_y are the currents in the compensation coils, and I_z is the one in the MOT+ coils. Since the MOT+ coil pair is much closer to the MOT center than the compensation coils, much smaller currents are needed for measurable displacement of the quadrupole trap, leading to the different scales in the two panels of fig. 4.

3.2 Absorption imaging and image processing

Imaging is performed with a single lens outside the vacuum chamber, under the 2f condition. This yields the real size of the image, meaning that the pixel size in the absorption imaging field-of-view is the physical size of the CCD pixels, i.e. 5.3 µm.

To determine the center-of-mass position of the atom cloud in the magnetic trap, we fit a two-dimensional Gaussian profile to the absorption image. In addition to the Gaussian core, the fit model includes a constant offset term to account for imperfections in the imaging process such as imperfect reference image and CCD dark current fluctuations. With these considerations, the fit is found to be robust, it converges reliably even with generic initial parameters.

To ensure that only reliable fits contribute to the statistical analysis, each image is subjected to a series of automated pre-registered quality-control checks. An image is retained only if all of the following conditions are met:

- uncertainty of the fitted cloud center $< 0.1 \,\mathrm{px} (\approx 0.5 \,\mathrm{\mu m})$,
- magnitude of residual skewness < 1,
- signal-to-noise ratio (Gaussian amplitude / constant offset) > 10.

In our experience, frames that fail these criteria occur in fewer than 1% of cases and can be traced to timing errors arising from transient communication glitches between the CCD camera and the control PC.

3.3 The effect of inhomogeneities

Identifying the spatial origin with the true center of the quadrupole, an inhomogeneous external field $\mathbf{B}_{\mathrm{ext}}(\mathbf{r})$ can be expanded in a Taylor series as

$$\mathbf{B}_{\text{ext}}(\mathbf{r}) = \mathbf{B}_{\text{ext}}(0) + \nabla \circ \mathbf{B}_{\text{ext}}|_{0} \mathbf{r} + \mathcal{O}(r^{2}). \tag{9}$$

The quadrupole field (2) can also be written in matrix form:

$$\mathbf{B}_{\mathbf{Q}}(\mathbf{r}) = \mathbf{Q}\,\mathbf{r}, \quad \text{with} \quad \mathbf{Q} \equiv Q \begin{pmatrix} 1 & 0 & 0 \\ 0 & 1 & 0 \\ 0 & 0 & -2 \end{pmatrix}. \tag{10}$$

Then, it is the sum of the external gradient matrix and the quadrupole matrix that determine the displacement of the magnetic zero point:

$$\mathbf{r}_0 = \left[\mathbf{Q} + \nabla \circ \mathbf{B}_{\text{ext}} \right]_0^{-1} \mathbf{B}_{\text{ext}}(0) \tag{11}$$

Even though the superposed field still grows linearly with distance from the center and retains a single magnetic zero, several prerequisites of the ideal buoy effect are lost already at this lowest order of inhomogeneity. Most importantly, \mathbf{r}_0 no longer simply flips sign upon reversing the sign of \mathbf{Q} , and the clean directional response to $\mathbf{B}_{\rm ext}(0)$ is also degraded. This is because, in contrast to the diagonal \mathbf{Q} , the external gradient matrix $\nabla \circ \mathbf{B}_{\rm ext}|_{\mathbf{r}=0}$ is generally non-diagonal.

The inhomogeneity of the stray field is contributed mainly by the ion pump and ion gauge, that are attached directly to the vacuum chamber and are hence relatively close to the MOT center in our setup. Moreover, the MOT+ coil pair being relatively close to the MOT center, the z-compensation field can also have inhomogeneities on the scale of interest, cf. section 3.4, which probably causes the larger uncertainty of the inferred magnetic centers in the z direction observed in figs. 2, 3 and 5.

3.4 Estimating the precision of simple approximations

The importance of magnetic trapping in cold-atom technology has long motivated the development of good approximate formulas for the trapping fields [54]. However, we can be numerically exact with the magnetic Python package [55] developed by our group. This package facilitates the calculation of static magnetic fields arising from arbitrary electromagnet configurations. We created a faithful representation of our electromagnet configuration within the package.

As a benchmark, we investigate the validity of the ideal quadrupole (2) in describing the actual field generated by the MOT coils. The comparison is shown in fig. 8. On the largest spatial scale of $0.1\,\mathrm{mm}~(\approx 20\,\mathrm{px})$ relevant to the displacement magnitudes in our experiment, the deviation from the ideal quadrupole shape is only at the micro-Gauss level. This is well below the sensitivity currently achievable with the buoy method, confirming that the simple quadrupole model is sufficient for interpreting displacement data at our present precision.

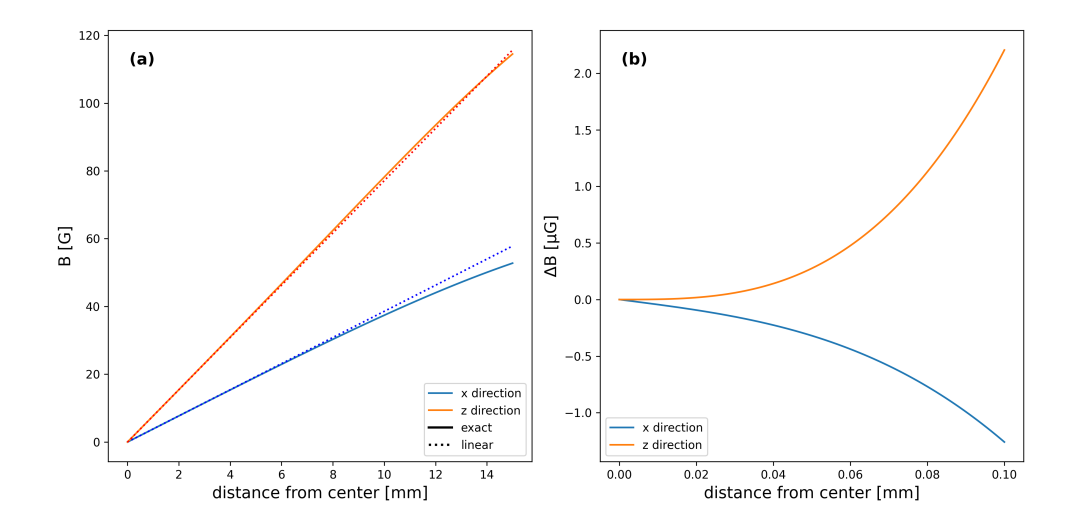


Fig. 8 Deviation of the magnetic field generated by the MOT coil pair from the ideal quadrupole form (2). (a) Comparison of the exact numerically computed field (solid lines) and the ideal quadrupole model (dotted lines), plotted along the horizontal (x, blue) and vertical (z, orange) axes. (b) Difference between the exact and linearized fields. The deviation remains below the micro-Gauss level within a 0.1 mm range around the trap center, supporting the validity of the quadrupole approximation at our current experimental resolution.

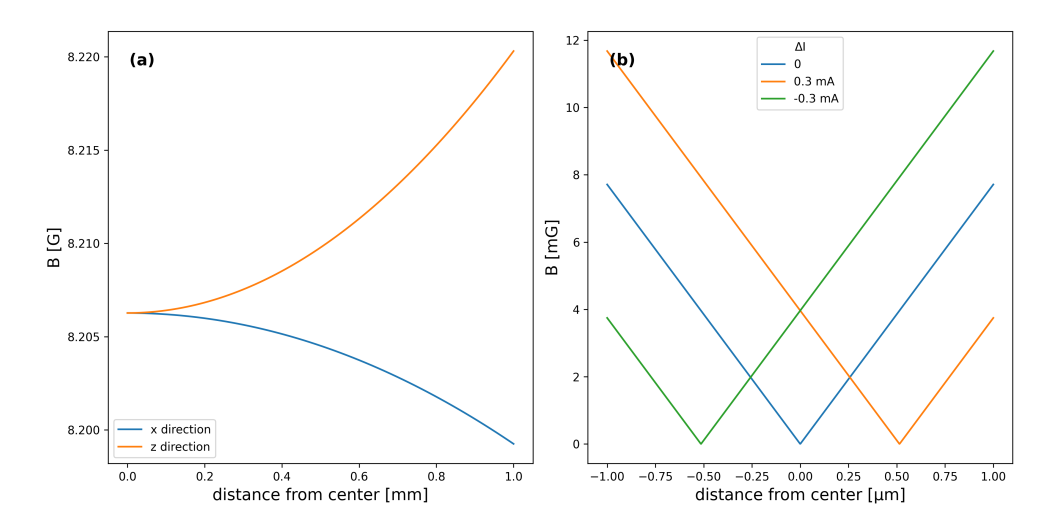


Fig. 9 (a) Deviation of the magnetic field generated by the MOT+ coils from perfect homogeneity. The field variation reaches the milli-Gauss scale within 0.1 mm of the trap center along the axial (z) direction. (b) Simulated effect of common-mode fluctuations in the current source driving the MOT coil pair. A variation of ± 0.3 mA around the nominal 4.7 A results in an axial displacement of approximately 0.5 µm in the magnetic potential minimum, corresponding to a shift of about 0.1 pixels.

Figure 9 illustrates two additional considerations relevant to the stability and accuracy of the buoy method. Panel (a) quantifies the inhomogeneity of the bias field produced by the MOT+ coil pair along the z-axis. Even though the coils are operated symmetrically, the proximity and geometric constraints introduce field curvature, resulting in variations of up to 1 mG over a spatial extent of 0.1 mm. This magnitude is already comparable to the sensitivity range of our current buoy implementation and plausibly explains the larger imperfections observed in the z-direction in section 2.2. Panel (b) examines the susceptibility of the trap center position to common-mode current fluctuations in the MOT coils. Our simulations show that even a 0.3 mA deviation induces less than a micron-scale displacement. Since our current sources have a stability on the order of 1 μ A, these results confirm that current noise contributes negligibly to the observed displacements.

4 Acknowledgments

This research was supported by the Hungarian National Research, Development and Innovation Office (Grant Nos. 2022-2.1.1-NL-2022-00004 and 2025-3.1.1-ED-2025-00011), the ERANET COFUND QuantERA programme (MOCA 2019-2.1.7-ERA_NET-2022-00041), the QuantERA II Programme (V-mag 2024-1.2.2-ERA_NET-2024-00012), and by the Swiss National Science Foundation (Grant No. 230870). AD and TWC acknowledges support from the János Bolyai research scholarship of the Hungarian Academy of Sciences.

5 Data availability

All absorption imaging data used in figs. 2 to 6 will be made publicly available in the HUN-REN ARP Research Data Repository.

References

- [1] Metcalf HJ, van der Straten P. Magnetic Trapping of Neutral Atoms. In: Laser Cooling and Trapping. vol. 40 of Graduate Texts in Contemporary Physics. Springer; 1999. p. 137–148.
- [2] Raab EL, Prentiss M, Cable A, Chu S, Pritchard DE. Trapping of Neutral Sodium Atoms with Radiation Pressure. Phys Rev Lett. 1987;59(23):2631–2634. https://doi.org/10.1103/PhysRevLett.59.2631.
- [3] Anderson MH, Ensher JR, Matthews MR, Wieman CE, Cornell EA. Observation of Bose-Einstein Condensation in a Dilute Atomic Vapor. Science. 1995;269(5221):198–201. https://doi.org/10.1126/science.269.5221.198.
- [4] Davis KB, Mewes MO, Andrews MR, van Druten NJ, Durfee DS, Kurn DM, et al. Bose–Einstein Condensation in a Gas of Sodium Atoms. Phys Rev Lett. 1995;75(22):3969–3973. https://doi.org/10.1103/PhysRevLett.75.3969.

- [5] Bloch I, Dalibard J, Zwerger W. Many-body physics with ultracold gases. Reviews of Modern Physics. 2008;80(3):885–964. https://doi.org/10.1103/RevModPhys. 80.885.
- [6] Jo GB, Shin Y, Will S, Pasquini TA, Saba M, Ketterle W, et al. Long Phase Coherence Time and Number Squeezing of Two Bose-Einstein Condensates on an Atom Chip. Physical Review Letters. 2007;98(3):030407. https://doi.org/10. 1103/PhysRevLett.98.030407.
- [7] Verdú J, Zoubi H, Koller C, Majer J, Ritsch H, Schmiedmayer J. Strong magnetic coupling of an ultracold gas to a superconducting waveguide cavity. Physical Review Letters. 2009;103(4):043603. https://doi.org/10.1103/PhysRevLett.103. 043603.
- [8] Petrich W, Anderson MH, Ensher JR, Cornell EA. Stable, tightly confining magnetic trap for evaporative cooling of neutral atoms. Phys Rev Lett. 1995;74(17):3352–3355. https://doi.org/10.1103/PhysRevLett.74.3352.
- [9] Reichel J, Hänsel W, Hänsch TW. Atomic Micromanipulation with Magnetic Surface Traps. Phys Rev Lett. 1999;83(17):3398-3401. https://doi.org/10.1103/ PhysRevLett.83.3398.
- [10] Fortágh J, Zimmermann C. Magnetic microtraps for ultracold atoms. Rev Mod Phys. 2007;79(1):235–289. https://doi.org/10.1103/RevModPhys.79.235.
- [11] Gehm M, O'hara K, Savard T, Thomas J. Dynamics of noise-induced heating in atom traps. Physical Review A. 1998;58(5):3914.
- [12] Greiner M, Bloch I, Hänsch TW, Esslinger T. Magnetic transport of trapped cold atoms over a large distance. Physical Review A. 2001;63(3):031401.
- [13] Folman R, Krüger P, Schmiedmayer J, Denschlag J, Henkel C. Microscopic atom optics: From wires to an atom chip. Advances in Atomic, Molecular, and Optical Physics. 2002;48:263–356. https://doi.org/10.1016/S1049-250X(02)80011-8.
- [14] Liu H, Peng S, Jiao B, Li J, Luo L. Ultra-low noise bipolar current source for ultracold atom magnetic system. Review of Scientific Instruments. 2023;94(5).
- [15] Kominis IK, Kornack TW, Allred JC, Romalis MV. A subfemtotesla multichannel atomic magnetometer. Nature. 2003;422(6932):596–599.
- [16] Dang H, Maloof AC, Romalis MV. Ultrahigh sensitivity magnetic field and magnetization measurements with an atomic magnetometer. Applied physics letters. 2010;97(15).
- [17] Sheng D, Li S, Dural N, Romalis MV. Subfemtotesla scalar atomic magnetometry using multipass cells. Physical review letters. 2013;110(16):160802.

- [18] Farooq M, Chupp T, Grange J, Tewsley-Booth A, Flay D, Kawall D, et al. Absolute magnetometry with He 3. Physical Review Letters. 2020;124(22):223001.
- [19] Buchner M, Höfler K, Henne B, Ney V, Ney A. Tutorial: Basic principles, limits of detection, and pitfalls of highly sensitive SQUID magnetometry for nanomagnetism and spintronics. Journal of Applied Physics. 2018;124(16).
- [20] Budker D, Kimball DFJ, editors. Optical Magnetometry. Cambridge University Press; 2013.
- [21] Rabi II, Zacharias JR, Millman S, Kusch P. A new method of measuring nuclear magnetic moment. Physical review. 1938;53(4):318.
- [22] Bell WE, Bloom AL. Optically driven spin precession. Physical Review Letters. 1961;6(6):280.
- [23] Kominis IK, Kornack TW, Allred JC, Romalis MV. A subfemtotesla multichannel atomic magnetometer. Nature. 2003;422:596–599. https://doi.org/10.1038/ nature01484.
- [24] Budker D, Romalis MV. Optical Magnetometry. Nature Physics. 2007;3:227–234. https://doi.org/10.1038/nphys566.
- [25] Allred JC, Kornack TW, Kominis IK, Romalis MV. High-sensitivity atomic magnetometer unaffected by spin-exchange relaxation. Physical Review Letters. 2002;89(13):130801. https://doi.org/10.1103/PhysRevLett.89.130801.
- [26] Shah V, Knappe S, Schwindt PDD, Kitching J. Subpicotesla atomic magnetometry with a microfabricated vapour cell. Nature Photonics. 2007;1:649–652. https://doi.org/10.1038/nphoton.2007.201.
- [27] Vengalattore M, Higbie JM, Leslie SR, Guzman J, Sadler LE, Stamper-Kurn DM. High-Resolution Magnetometry with a Spinor Bose-Einstein Condensate. Phys Rev Lett. 2007;98:200801. https://doi.org/10.1103/PhysRevLett.98.200801.
- [28] Afach S, Ayres NJ, Ban G, Bison G, Bodek K, Burghoff M, et al. A device for simultaneous spin analysis of ultracold neutrons and ¹⁹⁹Hg atoms. Phys Rev Lett. 2015;115(16):163002. https://doi.org/10.1103/PhysRevLett.115.163002.
- [29] Li X, Han B, Zhang K, Liu Z, Wang S, Yan Y, et al. All-optical dual-axis zero-field atomic magnetometer using light-shift modulation. Physical Review Applied. 2024;21(1):014023.
- [30] Castellucci F, Clark TW, Selyem A, Wang J, Franke-Arnold S. Atomic compass: detecting 3D magnetic field alignment with vector vortex light. Physical review letters. 2021;127(23):233202.

- [31] Bidel Y, Carraz O, Charrière R, Cadoret M, Zahzam N, Bresson A. Compact cold atom gravimeter for field applications. Applied Physics Letters. 2013;102(14).
- [32] Ehinger LH, Acharya BP, Barker DS, Fedchak JA, Scherschligt J, Tiesinga E, et al. Comparison of two multiplexed portable cold-atom vacuum standards. AVS Quantum Science. 2022;4(3).
- [33] Nshii C, Vangeleyn M, Cotter JP, Griffin PF, Hinds E, Ironside CN, et al. A surface-patterned chip as a strong source of ultracold atoms for quantum technologies. Nature nanotechnology. 2013;8(5):321–324.
- [34] Nichols CS, Nofs LM, Viray MA, Ma L, Paradis E, Raithel G. Magneto-optical trap with millimeter ball lenses. Physical Review Applied. 2020;14(4):044013.
- [35] Mcgilligan JP, Moore KR, Dellis A, Martinez G, de Clercq E, Griffin P, et al. Laser cooling in a chip-scale platform. Applied Physics Letters. 2020;117(5).
- [36] Hahn EL. Spin Echoes. Physical Review. 1950;80(4):580–594. https://doi.org/10.1103/PhysRev.80.580.
- [37] Ramsey NF. A Molecular Beam Resonance Method with Separated Oscillating Fields. Physical Review. 1950;78(6):695–699. https://doi.org/10.1103/PhysRev. 78.695.
- [38] Roussy TS, Caldwell L, Wright T, Cairncross WB, Shagam Y, Ng KB, et al. An improved bound on the electron's electric dipole moment. Science. 2023;381(6653):46–50.
- [39] Drever RW, Hall JL, Kowalski FV, Hough J, Ford G, Munley A, et al. Laser phase and frequency stabilization using an optical resonator. Applied Physics B. 1983;31(2):97–105.
- [40] Andrews MR, Townsend CG, Durfee DS, Miesner HJ, Kurn DM, Ketterle W. Observation of interference between two Bose condensates. Science. 1997;275(5300):637–641. https://doi.org/10.1126/science.275.5300.637.
- [41] Hueck K, Luick N, Sobirey L, Siegl J, Lompe T, Moritz H. High resolution imaging of ultracold fermions in microscopically tailored optical potentials. Review of Scientific Instruments. 2017;88(1):016103. https://doi.org/10.1063/1.4973564.
- [42] Krzyzanowska KA, Ferreras J, Ryu C, Samson EC, Boshier MG. Matter-wave analog of a fiber-optic gyroscope. Physical Review A. 2023;108(4):043305.
- [43] Zhu HY, Xue M, Li J, Deng M. Efficacy of differential phase extraction methods in dual atom interferometers under correlated noise conditions. Results in Physics. 2023;52:106855.

- [44] Zheng X, Dolde J, Kolkowitz S. Reducing the instability of an optical lattice clock using multiple atomic ensembles. Physical Review X. 2024;14(1):011006.
- [45] Thaprasop P, Zhou K, Steinheimer J, Herold C. Unsupervised outlier detection in heavy-ion collisions. Physica Scripta. 2021;96(6):064003.
- [46] Martin W, Mortlock D. An approach to robust Bayesian regression in astronomy. RAS Techniques and Instruments. 2025;4:rzaf035.
- [47] Maples M, Reichart D, Konz N, Berger T, Trotter A, Martin J, et al. Robust chauvenet outlier rejection. The Astrophysical Journal Supplement Series. 2018;238(1):2.
- [48] Huber PJ, Ronchetti EM. Chapter 3: The Basic Types of Estimates. In: Robust Statistics. John Wiley & Sons, Inc.; 2009.
- [49] Rodriguez-Nieva JF, Scheurer MS. Identifying topological order through unsupervised machine learning. Nature Physics. 2019;15(8):790–795.
- [50] Zhang YZ, Li F, Yun F. Integrating CBAM-CNN Architectures with K-means Clustering Algorithms for High-Efficiency and Accurate Metasurface Optical Properties Prediction. Applied Optics. 2025;.
- [51] Dose V. Bayesian inference in physics: case studies. Reports on Progress in Physics. 2003;66(9):1421.
- [52] Von Toussaint U. Bayesian inference in physics. Reviews of Modern Physics. 2011;83(3):943–999.
- [53] Varga D, Gábor B, Sárközi B, Adwaith K, Nagy D, Dombi A, et al. Loading atoms from a large magnetic trap to a small intra-cavity optical lattice. Physics Letters A. 2024;505:129444.
- [54] Bergeman T, Erez G, Metcalf HJ. Magnetostatic trapping fields for neutral atoms. Phys Rev A. 1987 Feb;35:1535–1546. https://doi.org/10.1103/PhysRevA. 35.1535.
- [55] Wigner Quantum Optics Group.: magnetic package. Available at https://github.com/WignerQuantumOptics/magnetic.